Dual-Wavelength Operation at 607 nm and 640 nm with the Same Threshold and Slope Efficiency in Pr³⁺:LiLuF₄ Crystal

Haotian Huang, Jing Xia *[ID], Nguyentuan Anh, Yuzhao Li and Yanfei Lü *[ID]

School of Physics and Astronomy, Yunnan University, Kunming 650500, China;
huanghaotian2000@sina.com (H.H.); nguyentuananh0930@163.com (N.A.); liyuzhao1992@163.com (Y.L.)
* Correspondence: xiajing_ynu@163.com (J.X.); optik@sina.com (Y.L.)

Abstract: A dual-wavelength (DW) Pr³⁺:LiLuF₄ (Pr:LLF) laser with the same threshold and slope efficiency was achieved for the first time. We theoretically deduced the conditions for obtaining the same threshold and slope efficiency of the DW operation, and experimentally demonstrated the orange-red DW Pr:LLF laser by optimizing the output coupling transmittance and adjusting the rotation angle of the intracavity Lyot filter. A CW orange-red DW laser, pumped by a 10 W 479 nm frequency-doubled optically pumped semiconductor laser (2ω-OPSL), delivers combined outputs of 607 nm and 640 nm with a total power of 2.69 W. The orange and red wavelengths maintained balanced power output under each pump level. Furthermore, by a type-I critical phase-matched (CPM) β-BaB₂O₄ (BBO) crystal, a CW ultraviolet (UV) second harmonic generation (SHG) at 312 nm was also obtained through intracavity sum-frequency mixing (SFM) of the 607 nm and 640 nm fundamental beams, achieving a maximum power output of 812 mW.

Keywords: dual-wavelength; visible laser; Pr³⁺:LiLuF₄ crystal; ultraviolet laser; solid-state laser

1. Introduction

The development of visible light sources has been promoted by activation mediums doped with trivalent rare earth (RE) ions (Pr³⁺, Sm³⁺, Dy³⁺, Eu³⁺, and Er³⁺), among which Pr³⁺ has a higher emission efficiency than other RE ions [1–7]. The breakthrough in high-power blue laser diode (LD) technology has led to the rapid development of lasers based on Pr³⁺ doped laser materials [8–14]. However, Pr³⁺ lasers mainly produce single-wavelength outputs, while there are few reports detailing the generation of DW lasers in Pr³⁺ doped materials. For example, we achieved the first CW visible DW laser in a Pr:YLF crystal with a total green power output of 324 mW (184 mW at 546 nm and 158 mW at 550 nm) in 2015. In 2022, Lin et al. reported a CW orange DW Pr:YLF laser at 604 nm and 607 nm with a total power output of 3.30 W [15]. In 2023, Jin et al. realized a CW orange DW emission at 604 nm (81 mW) and 607 nm (201 mW) in a Pr:YLF crystal [16]. Recently, we demonstrated a CW green DW emission at 546 nm and 550 nm with a total balanced power of 1.68 W in a Pr:LLF crystal [17]. Visible DW lasers serve as critical enablers in medical instrumentation and environmental monitoring. For glucose quantification, simultaneous green DW outputs facilitate hemoglobin derivative detection with enhanced accuracy by decoupling scattering effects [18]. In particular, orange-red DW emissions have emerged as versatile tools in advanced photonic systems with applications spanning precision sensing, medical diagnostics, and industrial processing [15,16,19].

Current reports on DW lasing in solid-state laser systems employ two distinct mechanisms: Stark splitting-induced energy level transitions within the single crystal [20–24] and

two birefringent crystals with perpendicular optical axes [25–27]. In DW lasers, an ongoing challenge lies in achieving a balance between the two output powers. Laser systems in a single crystal designed for DW operations typically include intracavity loss components such as precisely coated output couplers, birefringent filters, or etalons to adjust the losses of the two emission lines. However, the power outputs of the two emission lines could not remain balanced, which was due to gain competition between two transition wavelengths in an active medium [20]. The dual power outputs generated by the two active mediums could not always be maintained in balance, which was due to the competition of pumping in the two active mediums [25]. Although our latest research has achieved balanced control of DW power output, due to the need for precise adjustment of the intracavity loss elements (two etalons) at each pump level, this has affected the stability of the dual-wavelength laser system to a certain extent, and increased the complexity of the DW laser system [17]. We propose a novel approach to address this challenge, which enables the same threshold and slope efficiency across both operational wavelengths. As a result, the same power output was achieved at each pump power level.

Figure 1 presents the orange-red emission spectra of the *a*-cut Pr:LLF crystal in the 590–660 nm range, which can be calculated through the Fuchtbauer–Ladenburg equation [28] and was consistent with the emission spectrum initially measured by Cornacchia et al. [29]. The orange-red spectrum demonstrates that the two emission peaks were 607 nm ($^3P_0 \rightarrow {}^3H_6$ transition) and 640 nm ($^3P_0 \rightarrow {}^3F_2$ transition) in the π-direction, respectively. LiLuF$_4$ (LLF) exhibits isotypic crystallography with uniaxial LiYF$_4$ (YLF) [30]. The host lattice enables trivalent rare-earth substitution without necessitating charge compensation or structural modifications. Analogous to YLF, its refractive index demonstrates a negative thermal coefficient, reducing thermally induced defocusing while preserving comparable thermal expansion anisotropy across principal crystallographic directions [31]. Crucially, LLF undergoes complete congruent crystallization, contrasting with YLF incongruent solidification morphology. This phase-pure growth characteristic circumvents excess LiF addition, thereby preventing micro-inclusion formation that degrades optical performance.
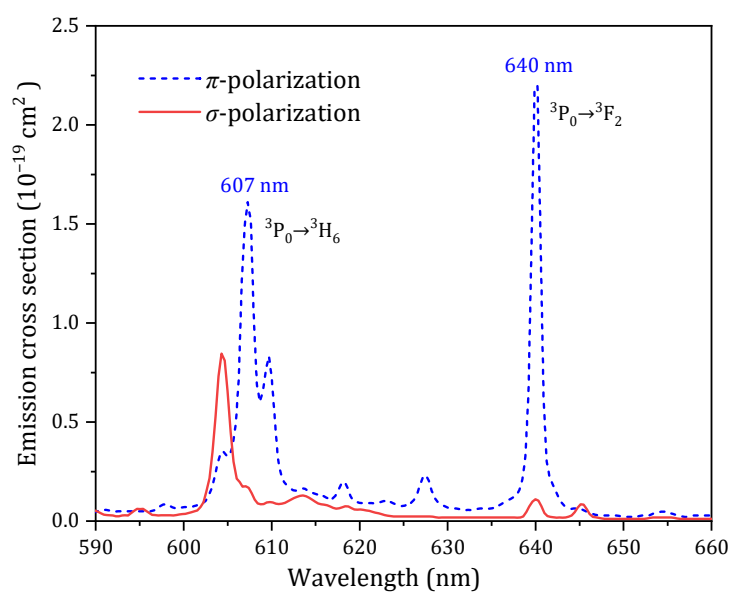
Figure 1. Emission spectra of the Pr:LLF crystal in the orange-red region.

In this work, an orange-red DW emission at 607 nm and 640 nm with the same threshold and slope efficiency was achieved in the Pr:LLF crystal. When 9.5 W of pump power was absorbed, a combined power output of 2.69 W was obtained. In addition, an SHG CW

UV laser emission at 312 nm was also obtained with a power output of 812 mW. CW UV lasers in the 300–320 nm region have been widely applied in key fields such as biomedical imaging, semiconductor photolithography-assisted exposure, real-time monitoring of environmental pollutants, and industrial precision micro-nano processing [32,33].

2. Theoretical Analysis

To make the same threshold and slope efficiency for the 607 nm and 640 nm wavelengths, we recall the laser output power ($P_{out,i}$) as described by [34] as follows:

$$P_{out,i} = \frac{\ln(1 - T_{oc,i})\eta_i}{\ln(1 - T_{oc,i}) - L_i}(P_{abs} - P_{tha,i}), \tag{1}$$

where the subscript $i = 607, 640$ means the 607 nm and 640 nm wavelengths, respectively, T_{oc} is the output coupling transmittance, L_i is the cavity round-trip loss, η_i is the quantum efficiency, P_{abs} is the absorbed power of 479 nm pump beam, and $P_{tha,i}$ is the laser oscillation threshold. Equation (1) further elucidates the functional dependence of slope efficiency ($\eta_{sa,i}$) on the pump power $\eta_{sa,i} = P_{out,i}/(P_{abs} - P_{tha,i})$, so the slope efficiency of each wavelength can be expressed as follows:

$$\eta_{sa,i} = \frac{\eta_i \ln(1 - T_{oc,i})}{\ln(1 - T_{oc,i}) - L_i}, \tag{2}$$

According to Equation (2), the condition of the some slope efficiency for 607 nm and 640 nm can be given as follows:

$$\frac{\eta_{607} \ln(1 - T_{oc,607})}{\ln(1 - T_{oc,607}) - L_{607}} = \frac{\eta_{640} \ln(1 - T_{oc,640})}{\ln(1 - T_{oc,640}) - L_{640}}, \tag{3}$$

From Equations (2) and (3), it can be concluded that changing $T_{oc,i}$ or L_i alone is unable to achieve equal slope efficiency for of the 607 nm and 640 nm wavelengths. For example, when $L_{640} > L_{607}$ and $P_{tha,640} = P_{tha,607}$, $\eta_{sa,607} > \eta_{sa,640}$ was obtained. Figure 2 shows the correlation of two slope efficiencies to achieve a greater understanding. Figure 2a describes the slope efficiencies of the 607 nm and 640 nm wavelengths at $P_{tha,640} = P_{tha,607}$, $L_{640} > L_{607}$, and $T_{oc,607} = T_{oc,640}$. It can be seen in Figure 2a that the absence of intersection points between the slope efficiency lines of the 607 nm and 640 nm wavelengths, so the two power outputs could not be balanced under any pumping conditions, as has been reported in ref. [35] for such slope efficiency characteristics. Similarly, the slope efficiencies of the 607 nm and 640 nm could not be equal when $P_{tha,640} > P_{tha,607}$, $L_{607} > L_{640}$, and $T_{oc,607} = T_{oc,640}$, as shown in Figure 2b, as has been reported in ref. [20]. For the same reason, when only the output coupling transmittance was changed, the slope efficiencies of the 607 nm and 640 nm could not be balanced, and the results in refs. [36,37] have been demonstrated.

Figure 2c shows the experimental effects when the transmittance at 607 nm and 640 nm was equal and the two loss elements were introduced into the cavity [17]. Although the slope efficiencies ($\eta_{sa,1} \neq \eta_{sa,2}$) of the emission wavelengths were difficult to achieve equally, the same power could be obtained through dynamic adjustment of the loss elements under specific pump power conditions. However, when pump power variations occur, precise micro-adjustment of the corresponding loss components becomes necessary to maintain power balance. This requirement for rigorous control introduces significant technical challenges, potentially limiting the practical application of DW laser systems. Therefore, in order to obtain the same slope efficiency, the output coupling transmittance and the cavity round-trip losses of 607 nm and 640 nm must be changed simultaneously. To achieve

different losses for the 607 nm and 640 nm, a Lyot filter was integrated into the cavity at θ_B (Brewster angle), as depicted in the inset of Figure 4. The rotation angle (β) is an angle between the optical axis of the Pr:LLF (C) and the projection of the incident light on the filter. The wavelength transmittance of the Lyot filter ($T_{Lyot,i}$) can be simplified as follows [38]:

$$T_{Lyot,i} = 1 - \frac{4\cos^2\beta\sin^2\theta_B}{1 - \cos^2\beta\cos^2\theta_B}\left(1 - \frac{\cos^2\beta\sin^2\theta_B}{1 - \cos^2\beta\cos^2\theta_B}\right)\sin^2(\delta/2), \tag{4}$$

where $\delta = 2\pi d(n_o - n_e)(1 - \cos^2\beta\cos^2\theta_B)/\lambda\sin\theta_B$ is the optical phase difference. d is the thickness of the filter, and n_o and n_e are the refractive index of o-light and e-light, respectively. It can be concluded, according to Equation (4), by rotating the Lyot filter, the transmittance of the emission wavelength will change. With Equation (4) and the following parameters: n_o = 1.5443, n_e = 1.5534, the round trip transmittance of the two emission wavelengths $T_{Lyot,i}^2$ was calculated as a function of the rotation angle β, as shown in the inset of Figure 3. The cavity round-trip loss $L_i = 1 - T_{Lyot,i}^2$.
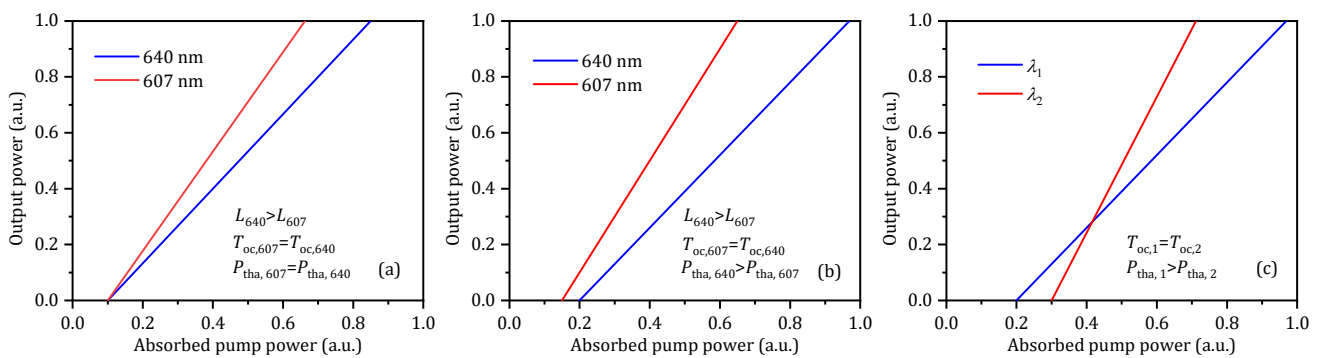
Figure 2. Schematic diagram of the slope efficiency for the two emission wavelengths. (**a**) $\eta_{sa,607} > \eta_{sa,640}$ at $L_{640} > L_{607}$, $T_{oc,607} = T_{oc,640}$, and $P_{tha,607} = P_{tha,640}$. (**b**) $\eta_{sa,607} > \eta_{sa,640}$ at $L_{640} > L_{607}$, $T_{oc,607} = T_{oc,640}$, and $P_{tha,640} > P_{tha,607}$. (**c**) $\eta_{sa}(\lambda_1) \neq \eta_{sa}(\lambda_2)$ at $T_{oc}(\lambda_1) \neq T_{oc}(\lambda_2)$ and $P_{tha}(\lambda_1) \neq P_{tha}(\lambda_2)$.
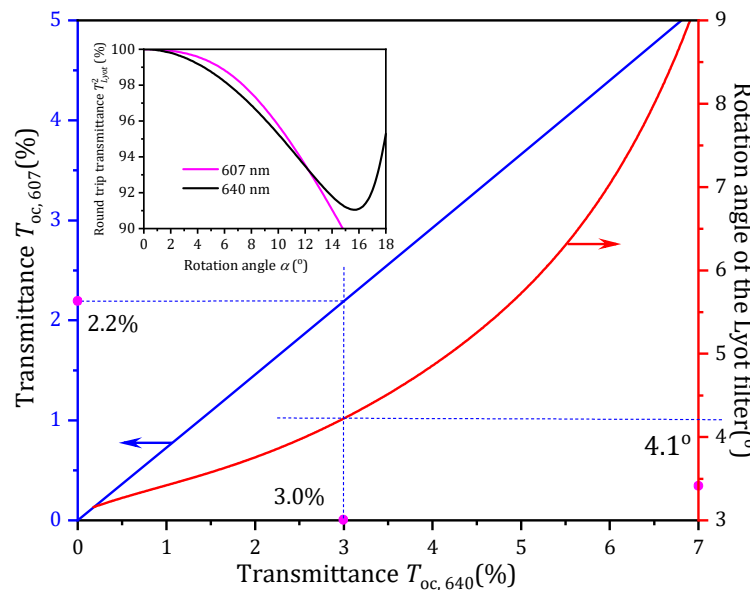
Figure 3. Dependence of (blue trace) the transmittance of the 607 nm $T_{oc,607}$ and (red trace) the rotation angle β on the transmittance of the 640 nm $T_{oc,640}$. Inset: the round trip transmittance of the two emission wavelengths T_{Lyot}^2 versus the rotation angle β.

When the power outputs of the 607 nm and 640 nm wavelengths are equal, the laser oscillation thresholds for the DW laser must also be equal. The threshold of each emission wavelength was described by [39] as follows:

$$P_{tha,i} = \frac{-\ln(1 - T_{oc,i}) + L_i}{2l_c\eta_i} \frac{h\nu_p}{\sigma_i\tau_i} \frac{1}{\iiint s_i(r,z)r_p(r,z)dv},$$

(5)

where l_c is the length of the active medium, $h\nu_p$ is the photon energy of the pump beam, τ_i is the upper energy level lifetime, σ_i is the stimulated emission cross section, $s_i(r,z)$ is the intensity distribution of the cavity mode for the laser wavelength, and $r_p(r,z)$ is the intensity distribution of the pump beam in the active medium. $s_i(r,z)$ and $r_p(r,z)$ can be respectively written as follows [40]:

$$s_i(r,z) = \frac{2}{\pi\omega_i^2 l_c} e^{2r^2/\omega_i^2},$$

(6)

and

$$r_p(r,z) = \frac{\alpha e^{-\alpha z}}{\pi\omega_p^2(z)(1 - e^{-\alpha z})} \Theta\left[\omega_p^2(z) - r^2\right],$$

(7)

where α is the absorption coefficient, ω_i is the laser spot radius, Θ is the Heaviside step function, and the pump beam size in the Pr:LLF crystal is described as follows:

$$\omega_p^2(z) = \omega_{p0}^2\left\{1 + \left[\frac{\lambda_p M_p^2}{n\pi\omega_{p0}^2}(z - z_0)\right]^2\right\},$$

(8)

where ω_{p0} is the pump spot radius, λ_p is the pumping wavelength, and M_p^2 is the quality factor of pump beam. It is worth mentioning that the laser spot radius (ω_i) was influenced by the thermal effect of the active medium and can be calculated based on ABCD matrix. The focal length of the thermal lens of the active medium can be expressed as follows [41]:

$$\frac{1}{f_{th,i}} = \frac{\xi_i\alpha P_{in}(dn/dT)_i}{\pi K_{c,i}} \int \frac{e^{-\alpha z}}{\omega_p^2(z)}dz$$

(9)

where ξ_i is the heat conversion coefficient, $(dn/dT)_i$ is the coefficient of the thermal chromatic dispersion, and $K_{c,i}$ is the thermal conductivity coefficient. According to Equations (1)–(9), under the parameters of the experiment: τ_i = 45.4 μs, α = 13 cm^{-1}, σ_{607} = 1.6 × 10^{-19} cm^2, σ_{640} = 2.2 × 10^{-19} cm^2, η_{607} = 0.79, η_{640} = 0.75, ω_{p0} = 100 μm, ξ_{607} = 21.1%, ξ_{640} = 25.2%, the transmittance $T_{oc,607}$ and the rotation angle β were calculated as a function of the transmittance $T_{oc,640}$, as shown in Figure 3. As shown in Figure 3, when DW lasers have the same slope efficiency and threshold, there exists a fixed correspondence between the transmittance of 607 nm and 640 nm wavelengths and the rotation angle β. For instance, in the experiment, the output coupler was used with $T_{oc,640}$ =3.0%, and only when $T_{oc,607}$ = 2.2%, and the corresponding rotation angle β was 4.1°, the slope efficiencies and the thresholds of the DW laser were simultaneously equal.

3. Experimental Setup

The schematic setup of the Pr:LLF orange-red DW laser is presented in Figure 4a. The pumping utilized a 2ω-OPSL emitting at 479 nm, delivering a maximum power output of 10 W and exhibiting a 3.5 quality factor of the beam (M²). The pump beam from the 2ω-OPSL was precision collimated using a lens (L_1) positioned at its output port. Subsequently, a 50 mm focal-length lens (L_2), antireflection (AR)-coated at 479 nm, enabled efficient focusing of the collimated beam into the Pr:LLF crystal.
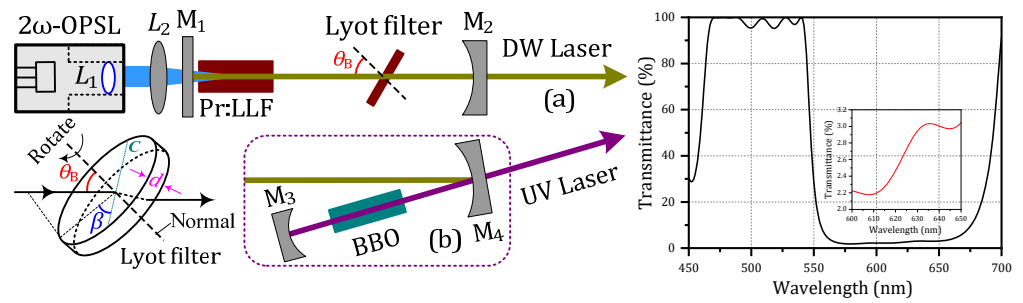
Figure 4. Schematic setups for (**a**) the Pr:LLF orange-red DW laser at 607 nm and 640 nm and (**b**) the SFM UV laser at 312 nm. Insert: Lyot filter. Right: transmittance curve of the M_2.

The plane mirror (M_1) served as the cavity input coupler, with an AR coating for 479 nm and high reflectivity (HR) coatings for 607 nm, 640 nm, and 312 nm. The plano-concave output coupler (M_2) with a radius of curvature ρ = −200 mm exhibited tailored transmittance properties: 2.2% at 607 nm, 3.0% at 640 nm. Three cavity output couplers featuring distinct transmittance (1.4% at 607 nm and 2.0% at 640 nm, 2.2% at 607 nm and 3.0% at 640 nm, and 2.9% at 607 nm and 4.0% at 640 nm) were utilized, with the M_2 configuration demonstrating superior performance metrics. The laser crystal was an *a*-axis-oriented Pr:LLF ($3 \times 3 \times 5$ mm^3, 0.2 at.% doping), which was AR coated at 312 nm, 607 nm, and 640 nm and was encapsulated in indium foil and secured to water-cooled copper mounts maintained at about 16 °C. A 0.4 mm-thick Lyot filter was utilized to adjust the losses of 607 nm and 640 nm.

4. Results and Discussion

First of all, a red single-wavelength emission was conducted without the Lyot filter to investigate the Pr:LLF laser performance. Figure 5 illustrates the dependence between the red output power of 640 nm and the pump power of 479 nm. The laser oscillation threshold was determined as 0.21 W. The red laser delivered a maximum power output of 5.02 W, corresponding to 9.5 W absorbed pump power (equivalent to 10 W incident pump power). This performance exhibited a slope efficiency of 56.1% and achieved an optical-to-optical conversion efficiency of 52.8% relative to the absorbed pump power. An optical spectrum analyzer was used, implementing data processing via dedicated spectral analysis software. The red spectrum under maximum pumping, as presented in the inset of Figure 5, exhibited a linewidth of 0.34 nm (FWHM) centered at 640.2 nm.
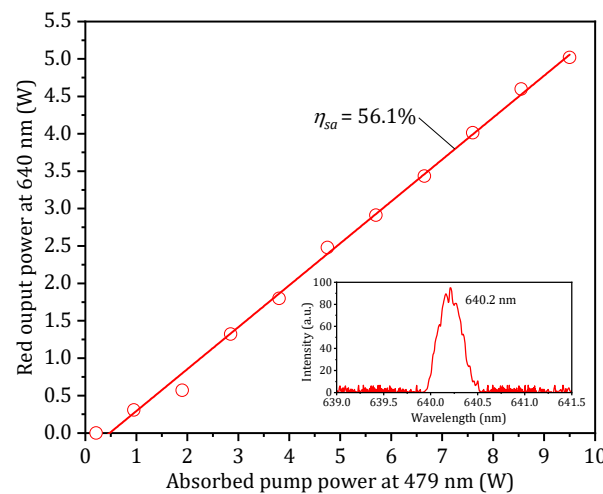
Figure 5. Red output power of 640 nm versus pump power of 479 nm. Inset: red laser spectrum at 640 nm under maximum pumping.

Then, to achieve the orange-red DW laser operation with the same threshold and slope efficiency, a Lyot filter was placed into the cavity. When the rotation angle β was adjusted to about 4°, a balanced output power was obtained, which was consistent with the calculation shown in Figure 3. The total power outputs at 607 nm and 640 nm versus 479 nm pump power are presented in Figure 6. The power balance of the orange and red wavelengths was sensitive to the adjustment in the pumping, but it could be reached to the equal output power by precisely adjusting the Lyot filter. The DW laser was separated by using a flexible wavelength selector, and the output power of each wavelength was measured, respectively. A CW total power output of 2.69 W was achieved under 9.5 W absorbed pumping. The orange-red DW laser demonstrated a 37.6% slope efficiency and 28.3% optical conversion efficiency relative to the absorbed pump power. The orange-red DW spectrum under maximum pumping is presented in the inset (a) of Figure 6. The peak wavelengths were 607.2 nm and 640.2 nm, with linewidths of 0.21 and 0.25 nm, respectively. The stability of the orange-red DW laser was measured with a power meter and the output power exhibited a stability of approximately 1.4% over a 1 h duration (Figure 7). The radii of the orange-red DW beam were measured along the x- and y-axes using the knife-edge technique, as illustrated in inset (a) of Figure 7, yielding values of $M_x^2 = 1.12$ and $M_y^2 = 1.16$. The beam profile was characterized in inset (a), which was close to the Gaussian function distribution.
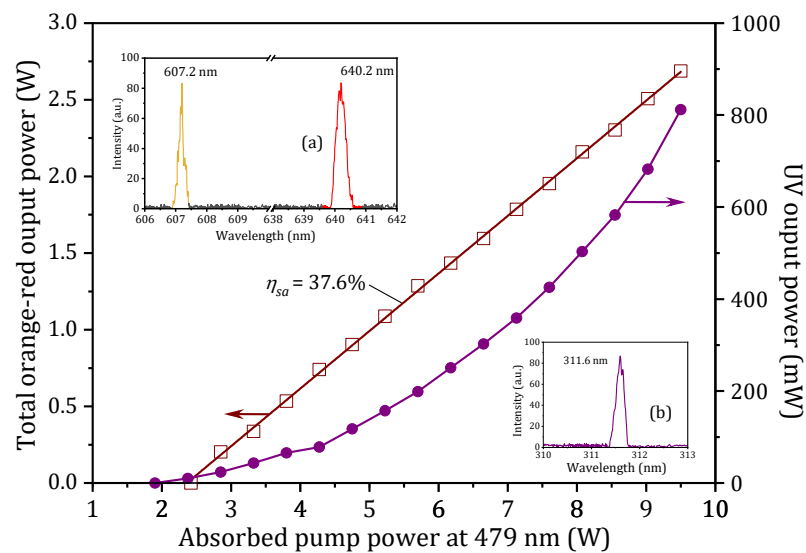
Figure 6. Total output powers of the orange-red DW laser and the UV laser versus absorbed pump power. Inset (**a**): output spectrum of the orange-red DW laser at 607 nm and 640 nm. Inset (**b**): output spectrum of the UV laser at 312 nm.

Finally, in order to obtain a CW UV laser output, a V-shaped cavity was utilized, as shown in Figure 4b. The other components were the same as shown in Figure 4a except the M_3 and M_4. The plano-concave mirror (M_3) with $\rho = -50$ mm was HR coated at 312 nm and 607 nm and 640 nm. The plano-concave mirror (M_4) with $\rho = -200$ mm was the UV output coupler, which was HR coated at 607 nm and 640 nm and AR coated at 312 nm. A BBO configured for type-I CPM ($\theta = 38.6°$ with $d_{eff} = 1.91$ pm/V) was employed as the nonlinear SFM crystal ($3 \times 3 \times 10$ mm^3). Figure 6 also illustrates the operational characteristics of the 312 nm UV laser. A CW SHG UV laser generated 812 mW output power with a threshold of 1.9 W, pumped at 9.5 W absorbed power. The UV spectrum under maximum pumping was presented in the inset (b) of Figure 6. The peak wavelength was 311.6 nm, with a linewidth of 0.21 nm. The UV power output exhibited a stability of approximately 2.3% over a 1 h duration (Figure 7). The beam radii of the UV laser were measured along the x- and y-axes,

as illustrated in inset (b) of Figure 7, yielding values of $M_x^2 = 1.27$ and $M_y^2 = 1.21$, while the beam profile is shown in the same inset (b).
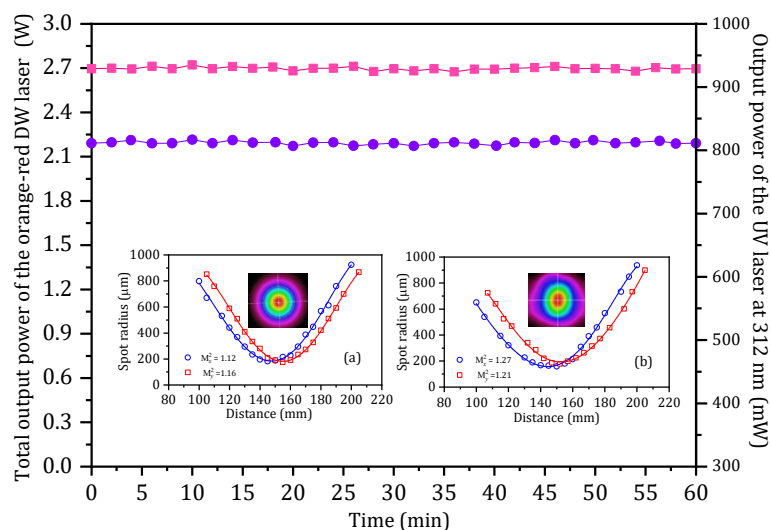
Figure 7. Stabilities of the orange-red DW laser (pink trace) and the UV laser (purple trace). Insets (**a**,**b**) show the X- and Y-axes radii as functions of Z-axis position for the orange-red and UV beams, respectively. The beam profiles of the orange-red DW laser and the UV laser were also shown in the insets (**a**,**b**).

5. Conclusions

A 2ω-OPSL-pumped CW orange-red DW Pr:LLF laser at 607 nm and 640 nm with the same threshold and slope efficiency was demonstrated. The conditions for obtaining the same threshold and slope efficiency of the DW operation were theoretically analyzed, and the orange-red DW laser in the Pr:LLF crystal was experimentally realized through optimizing the output coupled transmittance and adjusting the rotation angle of the intracavity Lyot filter. Under 10 W 2ω-OPSL pumping at 479 nm, an orange-red DW laser at 607 nm and 640 nm was realized with a total power output of 2.69 W. The 607 nm and 640 nm outputs maintained balanced power under varying pump levels. The total slope and optical conversion efficiencies were 37.6% and 28.3%, respectively. Furthermore, by a type-I CPM BBO crystal, an SHG CW UV at 312 nm was also obtained through intracavity SFM of the 607 nm and 640 nm fundamental orange-red beams, achieving a maximum power output of 812 mW. Orange-red DW lasers can achieve precise tissue treatment and disease diagnosis in the biomedical field, provide high-resolution material composition analysis in industrial inspection, and support cutting-edge applications such as gas molecule recognition and terahertz band generation in environmental monitoring and quantum optical research.

Author Contributions: Writing—original draft, H.H. and J.X.; writing—review and editing, Y.L. (Yuzhao Li); investigation, N.A.; project administration, Y.L. (Yanfei Lü). All authors have read and agreed to the published version of the manuscript.

Institutional Review Board Statement: Not applicable.

Informed Consent Statement: Informed consent was obtained from all subjects involved in this study.

Data Availability Statement: Data are contained within the article.

Conflicts of Interest: The authors declare no conflicts of interest.

References

1. Gün, T.; Metz, P.; Huber, G. Power scaling of laser diode pumped Pr^{3+}:LiYF$_4$ cw lasers: Efficient laser operation at 522.6 nm, 545.9 nm, 607.2 nm, and 639.5 nm. *Opt. Lett.* **2011**, *36*, 1002–1004. [CrossRef] [PubMed]
2. Chu, C.; Yang, X.; Wang, S.; Li, C.; Dong, Y. Diode-pumped orthogonally polarized Sm: YAP orange lasers with output power ratio and wavelength tuning. *Appl. Phys. B* **2025**, *131*, 62. [CrossRef]
3. Hansen, N.; Bellancourt, A.; Weichmann, U.; Huber, G. Efficient green continuous-wave lasing of blue-diode-pumped solid-state lasers based on praseodymium-doped LiYF$_4$. *Appl. Opt.* **2010**, *49*, 3864–3868. [CrossRef] [PubMed]
4. Lin, X.; Cui, S.; Ji, S.; Tian, Q.; Zhu, Y.; Li, W.; Xu, H.; Cai, Z. LD-pumped high-power high-efficiency orange vortex Pr^{3+}: YLF lasers. *Opt. Laser. Technol.* **2021**, *133*, 106571. [CrossRef]
5. Guo, H.; Yin, M.; Zhang, W. Upconversion of Er^{3+} Ions in LiKGdF$_5$: Er^{3+}, Dy^{3+} Single Crystal Produced by Infrared and Green Laser. *J. Rare Earth.* **2006**, *24*, 740–744.
6. Hadeethi, Y.A.; Kutbee, A.; Ahmed, M.; Sayyed, M.; Jagannath, G. Tuning of third-order nonlinear optical susceptibility of Eu^{3+} doped alkali borate glasses in visible region by embedding gold nanoparticles. *Eur. Phys. J. Plus* **2022**, *137*, 765. [CrossRef]
7. Lin, X.; Chen, M.; Feng, Q.; Ji, S.; Cui, S.; Zhu, Y.; Xiao, B.; Li, W.; Xu, H.; Cai, Z. LD-pumped high-power CW Pr^{3+}: YLF Laguerre-Gaussian lasers at 639 nm. *Opt. Laser. Technol.* **2021**, *142*, 107273. [CrossRef]
8. Dong, J.; Jin, L.; Jin, Y.; Dong, Y.; Yu, Y.; Jin, G. Direct generation of orthogonally polarized dual-wavelength double pulse Pr: YLF visible laser. *Appl. Phys. B* **2024**, *130*, 115. [CrossRef]
9. Baiocco, D.; Lopez-Quintas, I.; Vázquez de Aldana, J.R.; Tonelli, M.; Tredicucci, A. Comparative performance analysis of femtosecond-laser-written diode-pumped Pr:LiLuF$_4$ visible waveguide lasers. *Photonics* **2023**, *10*, 377. [CrossRef]
10. Xue, Y.; Dai, R.; Xu, H.; Cai, Z. High-power single-longitudinal-mode visible Pr:YLF ring lasers. *Opt. Laser Technol.* **2025**, *180*, 111495. [CrossRef]
11. Zhou, S.; Pan, Y.; Li, N.; Xu, B.; Liu, J.; Song, Q.; Xu, J.; Li, D.; Liu, P.; Xu, X. Spectroscopy and diode-pumped laser operation of Pr: LaMgAl$_{11}$O$_{19}$ crystal. *Opt. Mater.* **2019**, *89*, 14–17. [CrossRef]
12. Tian, Q.; Xu, B.; Li, N.; Luo, Z.; Xu, H.; Cai, Z. Direct generation of orthogonally polarized dual-wavelength continuous-wave and passively Q-switched vortex beam in diode-pumped Pr:YLF lasers. *Opt. Lett.* **2019**, *44*, 5586–5589. [CrossRef] [PubMed]
13. Dai, W.; Jin, L.; Liu, C.; Dong, Y.; Jin, G. 13.5 μj, 20 khz repetition rate, single frequency Pr^{3+}:YLF master oscillator power amplifier system. *Photonics* **2023**, *10*, 903. [CrossRef]
14. Zhang, S.; Wang, S.; Lian, G.; Wang, Z.; Yu, H.; Zhang, H. 7.56-W continuous-wave Pr^{3+}-based green laser via managing thermally induced effects. *Opt. Express* **2024**, *32*, 959–968. [CrossRef]
15. Lin, X.; Ji, S.; Feng, Q.; Liu, X.; Fang, R.; Xiao, B.; Li, W.; Xu, H.; Cai, Z. Heat-induced wavelength-switchable high-power CW orange Pr^{3+}:YLF lasers. *J. Lumin.* **2022**, *243*, 118627. [CrossRef]
16. Jin, L.; Jin, Y.; Yu, Y.; Dong, Y.; Jin, G. Orthogonally polarized dual-wavelength single longitudinal mode Pr:YLF laser at 607 nm and 604 nm. *Opt. Commun.* **2023**, *530*, 129180. [CrossRef]
17. Huang, H.; Xia, J.; Anh, N.; Li, Y.; Zhang, Y.; Zhang, Q.; Zhao, Z.; Lü, Y. Orthogonally Polarized Dual-Wavelength Pr:LLF Green Laser at 546 nm and 550 nm with the Balanced Output Powers at All Pump Power Level. *Photonics* **2025**, *12*, 393. [CrossRef]
18. Xia, J.; Lü, Y.; Liu, H.; Pu, X. Diode-pumped Pr^{3+}:LiYF$_4$ visible dual-wavelength laser. *Opt. Commun.* **2015**, *334*, 160–163. [CrossRef]
19. Kaneda, Y.; Tanaka, H.; Temyanko, V. Diode-pumped Sm:YLF laser at 605 nm and 648 nm. *Opt. Express* **2025**, *33*, 8903–8910. [CrossRef]
20. Huang, Y.; Cho, C.; Huang, Y.; Chen, Y. Orthogonally polarized dual-wavelength Nd: LuVO$_4$ laser at 1086 nm and 1089 nm. *Opt. Express* **2012**, *20*, 5644–5651. [CrossRef]
21. Du, E.; Zheng, H.; He, H.; Li, S.; Qiu, C.; Zhang, W.; Wang, G.; Li, X.; Ma, L.; Shen, S.; et al. Dual-wavelength confocal laser speckle contrast imaging using a deep learning approach. *Photonics* **2024**, *11*, 1085. [CrossRef]
22. Wang, S.; Li, C.; Li, Y.; Xia, J. Orthogonally polarized dual-wavelength Nd:LiYF$_4$ laser at 903 and 908 nm on $^4F_{3/2}\rightarrow^4I_{9/2}$ transition. *Opt. Laser Technol.* **2025**, *180*, 111510. [CrossRef]
23. Huang, H.; Li, Y.; Zhang, Y.; Zhang, Q.; Wang, S.; Li, C.; Dong, Y.; Xia, J. Research on output power ratio of dual-wavelength Nd:NaLa(WO$_4$)$_2$ laser on $^4F_{3/2}\rightarrow^4I_{13/2}$ transition. *Opt. Laser Technol.* **2025**, *181*, 112043. [CrossRef]
24. Waritanant, T.; Major, A. Dual-wavelength operation of a diode-pumped Nd:YVO$_4$ laser at the 1064.1 & 1073.1 nm and 1064.1 & 1085.3 nm wavelength pairs. *Appl. Phys. B* **2018**, *124*, 87.
25. Zheng, Y.; Zhong, K.; Qiao, H.; Zhang, X.; Li, F.; Sun, Y.; Wang, S.; Xu, D.; Yao, J. Compact, efficient and power-ratio tunable orthogonally polarized Nd:YVO$_4$ laser with coaxial diode-end-pumping configuration. *Opt. Commun.* **2022**, *523*, 128739. [CrossRef]
26. Lin, H.; Bao, S.; Liu, X.; Song, S.; Wen, Z.; Sun, D. Dual-wavelength continuous-wave and passively q-switched alexandrite laser at 736.7 nm and 752.8 nm. *Photonics* **2022**, *9*, 769. [CrossRef]

27. Liu, Y.; Zhong, K.; Mei, J.; Liu, C.; Shi, J.; Ding, X.; Xu, D.; Shi, W.; Yao, J. Compact and stable high-repetition-rate terahertz generation based on an efficient coaxially pumped dual-wavelength laser. *Opt. Express* **2017**, *25*, 31988–31996. [CrossRef]

28. Huber, G.; Krühler, W.; Bludau, W.; Danielmeyer, H. Anisotropy in the laser performance of NdP_5O_{14}. *J. Appl. Phys.* **1975**, *46*, 3580–3584. [CrossRef]

29. Cornacchia, F.; Richter, A.; Heumann, E.; Huber, G.; Parisi, D.; Tonelli, M. Visible laser emission of solid state pumped $LiLuF_4:Pr^{3+}$. *Opt. Express* **2007**, *15*, 992–1002. [CrossRef]

30. Ivanova, I.; Morozov, A.; Petrova, M.; Podkolzina, I.; Feofilov, P. Preparation and properties of single crystals of double fluorides of lithium and the rare earths. *Inorg. Mater.* **1975**, *11*, 1868.

31. Cornacchia, F.; Toncelli, A.; Tonelli, M. 2 μm Lasers with fluoride crystals: Research and development. *Prog. Quantum Electron.* **2009**, *33*, 61–109. [CrossRef]

32. Chen, X.; Shao, Y.; Yuan, J.; Zhang, D.; Wang, A. 303.5 nm cw Pr:BYF–BBO laser emission under 447 nm all-solid-state $Nd:GdVO_4$–BiBO blue laser pumping. *Laser Phys. Lett.* **2013**, *10*, 065002. [CrossRef]

33. Han, Y.; Guo, K.; Zhao, Y.; Xiong, M.; Wang, D.; Chen, J.; Cui, X.; Xu, B. Compact high-power 320-nm continuous-wave single-frequency laser based on power scaling of a diode-pumped $Pr:LiYF_4$ ring laser at red. *Opt. Lett.* **2024**, *49*, 3854–3857. [CrossRef]

34. Koechner, W. *Solid-State Laser Engineering*; Springer: Heidelberg, Germany, 2006.

35. Lü, Y.; Zhang, J.; Xia, J.; Liu, H. Diode-Pumped Quasi-Three-Level $Nd:YVO_4$ Laser with Orthogonally Polarized Emission. *IEEE Photon. Technol. Lett.* **2014**, *26*, 656–659. [CrossRef]

36. Li, P.; Li, D.; Li, C.; Zhang, Z. Simultaneous dual-wavelength continuous wave laser operation at 1.06 μm and 946 nm in Nd:YAG and their frequency doubling. *Opt. Commun.* **2004**, *235*, 169–174. [CrossRef]

37. Lünstedt, K.; Pavel, N.; Petermann, K.; Huber, G. Continuous-wave simultaneous dual-wavelength operation at 912 nm and 1063 nm in $Nd:GdVO_4$. *Appl. Phys. B* **2007**, *86*, 65–70. [CrossRef]

38. Wang, X.; Yao, J. Transmitted and tuning characteristics of birefringent filters. *Appl. Opt.* **1992**, *31*, 450–4507. [CrossRef]

39. Fan, T.; Byer, R. Diode laser-pumped solid-state lasers. *IEEE J. Quantum Electron.* **1988**, *QE-24*, 895–912. [CrossRef]

40. Chen, Y. cw dual-wavelength operation of a diode-pumped $Nd:YVO_4$ laser. *Appl. Phys. B* **2000**, *70*, 475–478. [CrossRef]

41. Zheng, Y.; Zhong, K.; Liu, K.; Qiao, H.; Zhang, X.; Xu, D.; Yao, J. Thermal effects of diode-end-pumped dual-wavelength solid-state lasers with coaxially arranged dual laser crystals. In *Advanced Lasers, High-Power Lasers, and Applications XII*; SPIE: Paris, France, 2021; pp. 51–61.